

Received 17 June 2023; Accepted 30 October 2023
<https://doi.org/10.22226/2410-3535-2023-4-382-386>



Local conductivity of thermobarically sintered detonation nanodiamond

V. A. Plotnikov, S. V. Makarov, D. G. Bogdanov[†], A. S. Bogdanov

[†]bogdanov.d.g@mail.ru

Altai State University, Barnaul, 656049, Russia

Abstract: Analysis of volt-current dependences discovered in thermobarically sintered detonation nanodiamond composites is covered in the paper. Composite nanodiamond materials were obtained in the course of sintering at the press-free high-pressure apparatus (BARS) under 5 GPa and at temperatures 1300, 1400 and 1500°C. Volt-current dependences are non-linear and show a zero-current area in the voltage interval from –3 to +1 V. Non-linear character of the volt-current dependences is connected with the structural state of the detonation diamond non-diamond carbon shell having a graphite-like onion-shaped structure and composed of 2–3 graphene planes about 1 nm thick. It is just the state of the electronic sub-system of such minimum package of graphene planes that stipulates charge carrier tunneling in the current channel under voltage application between the conducting probe and the sample, as well as it defines specific non-linearity of volt-current dependences with the zero-current area.

Keywords: detonation nanodiamond, thermobaric sintering, probe microscopy, local conductivity

1. Introduction

High hardness that can reach 80–130 GPa in certain diamond types [1], and high thermal conductivity that achieves 2200 W/(mK) in diamond monocrystals [2] are among unique properties of diamond materials. The combination of such properties makes it possible to consider diamond as an advanced material for obtaining high strength composite materials, as well as effective heat-sinking panels operating under increased thermal and mechanical loads. Difficulty of diamond scaffold forming [3] which is conditioned by the presence of the impurities-bearing elaborate shell of the nanodiamond particles [4,5] has still been a challenge for applying detonation nanodiamond in manufacturing high strength composites. Impurity shell consists of carbon nondiamond phase [5], but also of metallic impurities and volatile compounds that play a decisive role in the process of nanodiamond particles aggregation [4].

More detailed data on the nanodiamond cluster structure (X-ray results) show that detonation nanodiamond consists of carbon diamond phase (diamond core) with its specific crystal lattice and amorphous carbon phase on its surface [6,7]. The thickness of the nondiamond carbon layer does not exceed 1.5 nm and is in the range between 0.5–1.5 nm [6]. The carbon layer adjacent to the diamond core looks as if it is made of the flakes that form the onion-like structure [7], with graphite nanosheets and graphite particles impregnated into it. Another model shows that there are layered graphene structures on the nanodiamond surface that totally cover the diamond core surface [8]. Thus, nondiamond amorphous phase is in fact an array of various carbon phases and their structural state has still been unclear and needs further studying.

At room temperature nanodiamond demonstrates good dielectric properties [9]. In spite of the fact that carbon nondiamond phase is water-resistant, it can be observed that on the surface nanopores are able to adsorb sufficient amounts of water [10] that determine the electrophysical properties of such system [11].

Study of the detonation diamond electrophysical properties demonstrates that nanocrystalline diamond contains quantum effects peculiar for low-size systems, such as high charge drift velocity and electron-emission properties linked to the negative electron affinity typical of wide-band semiconductors [12]. For instance, covering molybdenum electrode with nanodiamond film results in dramatic (practically 50%) drop of voltage threshold of electron autoemission [13]. It is noteworthy that low operating voltage of electron autoemission in carbon diamond-like thin films are stipulated by the decreased operational effect of the output [12]. This goal is effectively achieved by using diamond-like films with ordered and highly symmetrical island structure [12,14] that provides nanoscale hexagonally-ordered and close-packed array of high-density emission centers [14].

As for conductivity of the thermobarically sintered nanodiamond, it is apparently associated with the structural state of the carbon nondiamond phase on the diamond core surface. Actually, exploring temperature dependence of nanodiamond-pyroc carbon composite carbon material that had been bombarded by neutrons manifests its semiconducting properties [15] and the pyroc carbon leading role in formation of the material electrophysical properties. Pyroc carbon on the nanodiamond surface presents a quasis two-dimensional graphite-like structure with the majority of carbon atoms consolidated by sp^2 -bonds. It should be stressed

that currently there is still no physical comprehension of charge transfer mechanisms in similar nano-sized carbon-carbon composites, but it might be proposed that conductivity of such carbon composite is conditioned by carriers transfers between broken and distorted onion-type structure layers [16].

Analysis of the publications shows that major vector of investigations is focused mainly on studying detonation diamond emission properties. This paper presents analysis of thermobarically sintered nanodiamond composites local conductivity and its relation to the structural state of nanodiamond core carbon shell.

2. Materials and experimental methods

Detonation nanodiamond powder produced by “Altai” Federal Research & Production Center in compliance with technical specification 84-1124-87 was used in the research. Thermobaric sintering of nanodiamonds was fulfilled at high-pressure multi-anvil “split-sphere” apparatus (BARS). High-pressure cell was manufactured of refractory oxides ZrO_2 and CaO with tubular graphite-like heater. Instrument error in measuring pressure and temperature in the experiments was taken as ± 0.2 GPa and $\pm 25^\circ C$, respectively. Sintering mode in all our experiments was unaltered: pressure increasing in the apparatus, then heating the sample under study, 60-second exposition at maximum p - T parameters and fast cooling. Sintering was implemented under pressure 5 GPa and at temperatures 1300, 1400 and $1500^\circ C$. To conduct the experimental thermobaric sintering, some disks having 8 mm in diameter were fabricated of the detonation nanodiamond initial powder. Then capsules of the refractory MgO oxide were fabricated. Before starting the experiment, the sample was put into the capsule to be dried at $120^\circ C$. After the sintering procedure, the capsule was dissolved in concentrated HNO_3 to release the sample. Application of this method provided sintering the sample having the volume more than 250 mm^3 .

Study of the structural state of the nanodiamond composite structural state and measuring volt-current dependences were conducted with application of Solver Next scanning probe microscope. Local electrophysical properties were measured using the method for displaying spreading resistance and electro-force spectroscopy. Measurements were made at the surface regions having globular structure and high conductivity.

X-ray diffraction examining of the samples was conducted on DRON-3 diffractometer with an X-ray copper anode tube. X-ray patterns were obtained in the 2θ 25° – 100° angle interval in the discrete scanning mode with 0.01 spacing and 3.6 sec spacing exposition.

Figure S1 (supplementary material) gives the chart that explains the equipment and methods used in the experiments.

3. Results and discussion

The structure of the thermobarically sintered detonation diamond is shown in Fig. 1.

Local electricity-conducting properties were defined exactly for this kind of globular structure. Table 1 shows

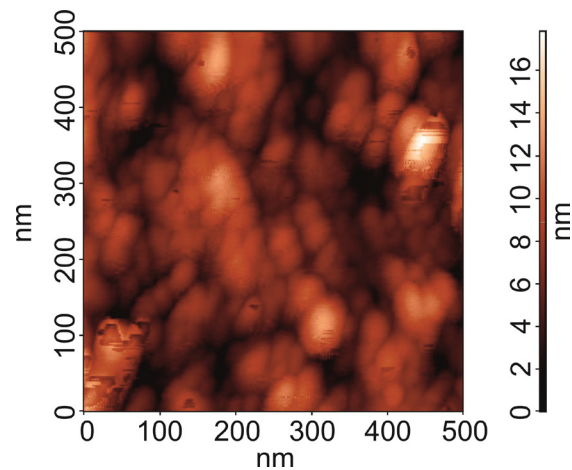


Fig. 1. (Color online) The structure of the thermobarically sintered detonation diamond.

Table 1. Conductivity of the thermobarically sintered nanodiamond.

Temperature, $^\circ C$	Pressure, GPa	Results of probe scanning of the surface and measurements of spreading current
1300	5	Conducting areas are absent
1400	5	Conducting areas are poorly-expressed
1500	5	Vast conducting areas

parameters of thermobaric sintering and local conducting properties of the sintered nanodiamond composites.

As it is obviously seen from the data above, well-expressed conducting properties are discovered only in the composite thermobarically sintered at $1500^\circ C$. Conducting areas are absent in the sample sintered at $1300^\circ C$. And the sample sintered at $1400^\circ C$ demonstrates only point poorly-expressed conducting areas.

Figures 2 a and 3 a present local volt-current dependences received in the marked measuring points on the composite surface. The surface structure of the composite sintered at $1500^\circ C$ shown in Figs. 2 b and 3 b is characterized by globular structure (Fig. 2 b) and vast areas with pronounced conductivity shown in Fig. 3 b as a light-coloured region about $10\text{ }\mu m$ in size. Local points for measuring local conductivity were selected just in this region.

It follows from the data observed in Figs. 2 and 3 that volt-current dependences are characterized by evidently expressed non-linearity that is presented by a zero current area in the voltage interval approximately from -0.5 to $+0.5\text{ V}$ (Fig. 2 a) and from -3 to $+1\text{ V}$ (Fig. 3 a). That means that the zero current area in Fig. 3 a is asymmetrical to the zero voltage.

This is an instrumental error made when measuring the volt-current dependence. Detonation nanodiamond is known to manifest its good dielectric properties that are verified by the low angle tangent of dielectric losses [17]. It is the adsorbed water that might be a stipulating factor of the discovered conductivity of the detonation nanodiamond, as was demonstrated above [10–11]. The conductivity effect relates to water ionization and formation of hydronium ions (H_3O^+) as charge carriers, i.e. conductivity is determined

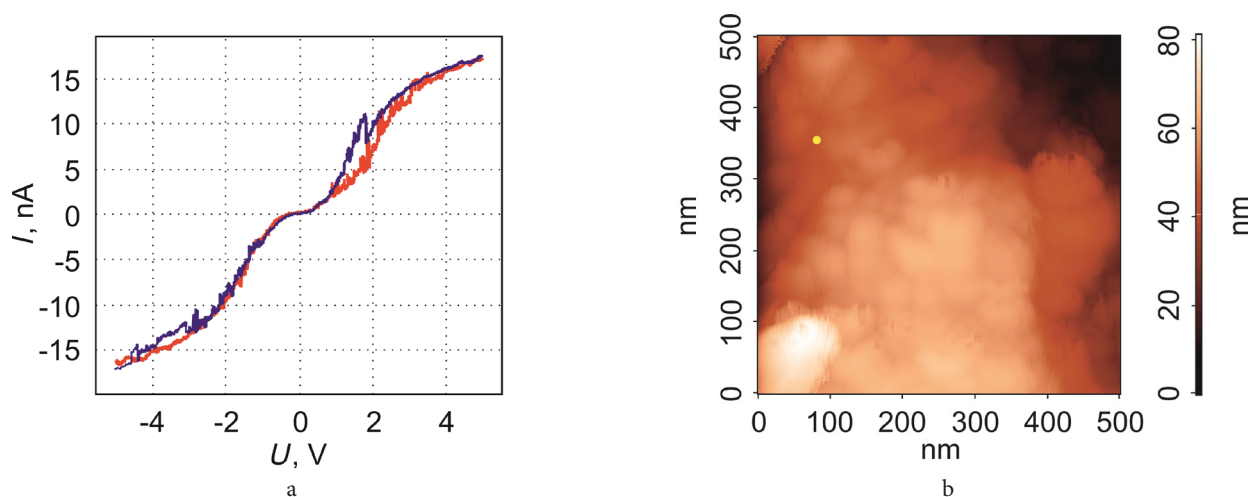


Fig. 2. (Color online) Local non-linear volt-current dependence in thermobarically sintered at 1500°C detonation nanodiamond with a zero-current area in the voltage interval from -0.5 V and approximately up to $+0.5$ V (a). The structure of the sample fragment with location of volt-current dependence measuring point (b).

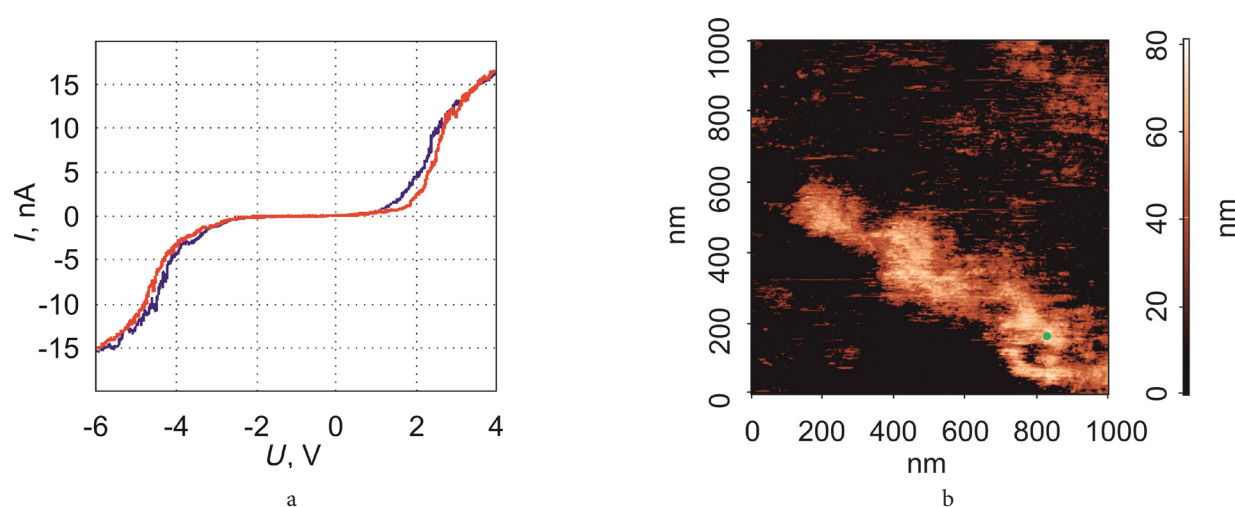


Fig. 3. Local non-linear volt-current dependence in thermobarically sintered at 1500°C detonation nanodiamond with a zero-current area in the voltage interval from -3.0 V and approximately up to $+1.0$ V (a). The structure of the sample fragment with vast conducting areas (light-coloured areas) with location of volt-current dependence measuring point (b).

by the protons charge transfer [10]. It is evident that this conductivity mechanism is absent in our samples after their thermobaric sintering at 1500°C and under pressure of 5 GPa. Hydrating of the detonation nanodiamond cannot determine the conductivity mechanism in our samples either [18]. Formation of the strongly-linked with the diamond core hydrogen layer on the diamond particle surface results in emerging the hydrated diamond surface conductivity that is determined by the vertex of the valence band shift higher than Fermi energy with density increase of the surface C-H groups.

Meanwhile, onion-like structures that were obtained as the result of detonation diamond annealing in high vacuum demonstrate high electric conductivity [19]. In this case, the onion-like structure features either the closed multi-layer graphene shells, or nanodiamond particle cores, or wholly graphitized particles at high-temperature annealing of detonation nanodiamond.

As the publication [16] states, conductivity of nanodiamond-pyroc carbon composite carbon material is conditioned by carriers transfers between broken and distorted onion-like graphene layers. Our samples

demonstrate that formation of this onion-like structure of the carbon surface layer in the process of thermobarical sintering goes simultaneously with the diamond core growing [20]. As it is shown (see Fig. 4), the sample sintered at 1500°C demonstrates wide, evidently expressed reflexes at the angles $2\theta = 26.5^\circ$ and $2\theta = 77.6^\circ$ [21], that correspond to the diffraction on graphite planes (002) and (110) [22]. As for the X-ray patterns of other samples — nanodiamond initial powder, as well as sintered at temperatures 1300 and 1400°C — graphite reflex (002) is not observed.

The crystals with hexagonal structure that are formed of separate graphene layers placed parallel to each other and at equal distances but subjected to random turning from the normal to the layers, will show only type (001) and type ($hk0$) reflections in the X-ray patterns. Presence of only 001 and $hk0$ reflections and absence of hkl reflections points at the absence of 3D periodicity of hexagonal planes positioning in the structure of the nanodiamond crystal graphite-like shell. In fact, this layer features disordered unclosed graphite-like structures, so-called “onion-like” carbon structures consisting of graphene nanoplates [22, 23].

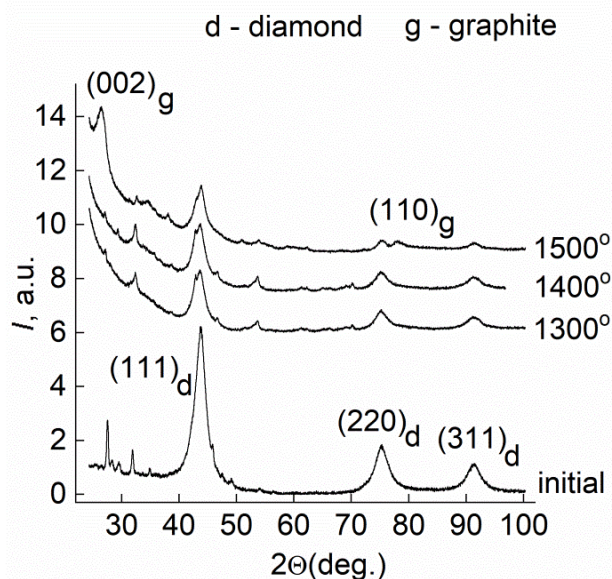


Fig. 4. X-ray patterns of nanodiamond composites thermobarically sintered at temperatures 1300, 1400, 1500°C and 5 GPa pressure. The initial powder X-ray pattern shows major reflexes.

The broadening of the diffraction maxima can be due to the small size of the coherent scattering areas (crystallites). In addition, crystal lattice defects, which cause the atoms displacement in the crystal lattice, lead to broadening of the diffraction peaks. The value of the broadening associated with the micro-deformation of the lattice is determined by the value $\Delta d/d$. Here Δd is the average change of the interplanar distance and d is the interplanar distance in the perfect crystal.

Since the elastic moduli are large in nanodiamond crystals, the value $\Delta d/d$ cannot be large. Therefore, to determine the size of crystallites D , we can use the simplified formula according to which the broadening of X-ray reflections is related only to the small size of the crystals:

$$D = \frac{\lambda}{\beta \cos \theta}.$$

Evaluation of these carbon structures size based on the analysis of reflection widening (002) showed that their size is about 7.8 nm. It is evident that such size of carbon inclusions cannot be linked with the diffraction on the carbon particles of similar size. The graphite phase of this size that manifested itself in our case can be positioned only on the surface of the diamond core. Actually, the value of 7.8 nm correlates with the size of the diamond complex that consists of the diamond core having the size of 6.9 nm and carbon structures surrounding the diamond nanocrystal. That is, this carbon shell thickness is about 0.9 nm. The calculated value of the interplanar spacing makes $d(002) = 3.36 \text{ \AA}$ that is in good agreement with the period of the neighbouring graphene layers arrangement in graphite perfect crystal structure [24–27]. So, the diamond core carbon shell (onion-like structure) consists of 2–3 graphene layers that are disoriented with respect to each other.

It is this kind of graphene structures where special state of the electron subsystem of π -electrons [25] is discovered, with these electrons presented as Dirac conical bodies shifted

against each other in Brillouin zone and stipulating tunneling of electrons from the filled states of Dirac conical bodies into their empty states [26,27], as well as non-linearity of volt-current dependence as is shown in Figs. 2 a and 3 a. Thus, zero current presence within certain voltage interval from –3 to +1 V (Fig. 3 a) in thermobarically sintered nanodiamond material points at the existence of electron tunneling through dielectric interlayer in the process of current channel formation in the chain of nanodiamond crystals with graphite-like shells.

4. Conclusions

The structural state and local conductivity of the thermobarically sintered nanodiamond composite were studied. Non-linear volt-current dependences with a zero current area have shown their relation with the structural state of carbon surface layer formed by 2–3 graphene planes assembled in an onion-shaped structure with these planes disoriented with respect to each other so that their new positions differ from the positions in the ideal graphite crystal. The state of the electron subsystem of such laminated structure is a crucial factor of electrophysical properties of the nanodiamond composite that manifest themselves in charge carrier tunneling when electric voltage is applied between the probe and the sample.

Supplementary material: The online version of this paper contains supplementary material available free of charge at the journal's website (lettersonmaterials.com).

References

1. H. Sumiya, N. Toda, S. Satoh. *Diamond & Related Materials*. 6, 1841 (1997). [Crossref](#)
2. J.R. Olson, R.O. Pohl, J.W. Vandersande, A. Zoltan, T.R. Anthony, W.F. Banholzer. *Phys. Rev. B*. 47, 14850 (1993). [Crossref](#)
3. P.A. Vityaz, V.T. Senyut. *Phys. Solid State*. 46, 743 (2004). (in Russian)
4. D.G. Bogdanov, V.A. Plotnikov, S.V. Makarov, A.S. Bogdanov, A.A. Chepurov. *Izv. Vyssh. Uchebn. Zaved. Khim. Khim. Tekhnol.* 62, 25 (2019). (in Russian) [Crossref](#)
5. I.I. Kulakova. *Phys. Solid State*. 46, 636 (2004). [Crossref](#)
6. M.V. Baidakova, A.Y. Vul', V.I. Siklitskii, N.N. Faleev. *Phys. Solid State*. 40, 715 (1998). [Crossref](#)
7. A.E. Aleksenskii, M.V. Baidakova, A.Y. Vul', V.I. Siklitskii. *Phys. Solid State*. 41, 668 (1999). [Crossref](#)
8. E.M. Baitinger, E.A. Belenkov, M.M. Brzhezinskaya, V.A. Greshnyakov. *Phys. Solid State*. 54, 1715 (2012). [Crossref](#)
9. A. Chaudhary, J.O. Welch, R.B. Jackman. *Appl. Phys. Lett.* 96, 242903 (2010). [Crossref](#)
10. E.-Z. Pica-Salazara, K. Sagisakab, Y. Hattorib, et al. *Chemical Physics Letters*. 737, 100018 (2019). [Crossref](#)
11. G.A. Sokolina, S.A. Denisov. *Izv. Vyssh. Uchebn. Zaved. Khim. Khim. Tekhnol.* 56, 70 (2013). (in Russian)
12. R.K. Yafarov, N.M. Kotina. *Basic Problems of Material Science*. 13, 534 (2016). (in Russian)

13. V.V. Zhirnov, O.A. Shenderova, D.L. Jaeger, T. Tyler, D.A. Areshkin, D.W. Brenner, J.J. Hren. Phys. Solid State. 46, 657 (2004). [Crossref](#)
14. V.A. Plotnikov, B.F. Dem'yanov, S.V. Makarov, A.I. Zyryanova. Technical Physics Letters. 45, 359 (2019). [Crossref](#)
15. S.K. Gordeev, R.F. Konopleva, V.A. Chekanov, S.B. Korchagina, S.P. Belyaev, I.V. Golosovskii, I.A. Denisov, P.I. Belobrov. Phys. Solid State. 55, 1480 (2013). [Crossref](#)
16. S.K. Gordeev, P.I. Belobrov, N.I. Kiselev, E.A. Petrakovskaya, T.C. Ekstrom. MRS Online Proceedings Library. 638, 14161 (2000). [Crossref](#)
17. A. Chaudhary, J.O. Welch, R.B. Jackman. Appl. Phys. Lett. 96, 242903 (2010). [Crossref](#)
18. T. Kondo, I. Neitzel, V.N. Mochalin, J. Urai, M. Yuasa, Y. Gogotsi. Journal of Applied Physics. 113, 214307 (2013). [Crossref](#)
19. M. Zeiger, N. Jäckel, D. Weingarth, V. Presser. Carbon. 94, 507 (2015). [Crossref](#)
20. D.G. Bogdanov, V.A. Plotnikov, S.V. Makarov, A.S. Bogdanov, A.P. Yelissev, A.A. Chepurov, E.I. Zhimulev. Letters on Materials. 11, 485 (2021). (in Russian) [Crossref](#)
21. D.G. Bogdanov, A.S. Bogdanov, V.A. Plotnikov, S.V. Makarov, A.P. Yelissev, A.A. Chepurov. RSC Adv. 11, 12961 (2021). [Crossref](#)
22. D. Reznik, C.H. Olk, D.A. Neumann, J.R. D. Copley. Phys. Rev. B. 52, 116 (1995). [Crossref](#)
23. S. Tomita, A. Burian, J.C. Dore, D. LeBolloch, M. Fujii, S. Hayashi. Carbon. 40, 1469 (2002). [Crossref](#)
24. A.R. Ubbelohde, F.A. Lewis. Graphite and its cristal compounds. Moscow, Mir (1965) 256 p. (in Russian)
25. T. Enoki. Phys. Solid State. 46, 651 (2004). [Crossref](#)
26. E.E. Vdovin, Yu.N. Khanin. JETP Letters. 108, 641 (2018). (in Russian) [Crossref](#)
27. S.V. Morozov, K.S. Novoselov, A.K. Geim. Physics — Uspekhi. 178, 776 (2008). (in Russian) [Crossref](#)

Ссылки 9 и 17 совпадают. Внесите необходимые изменения. При отсутствии ответа ссылка будет удалена, нумерация изменена, в том числе и в тексте.

Ссылка 27 - DOI (Crossref) заменен на DOI представленной русскоязычной версии

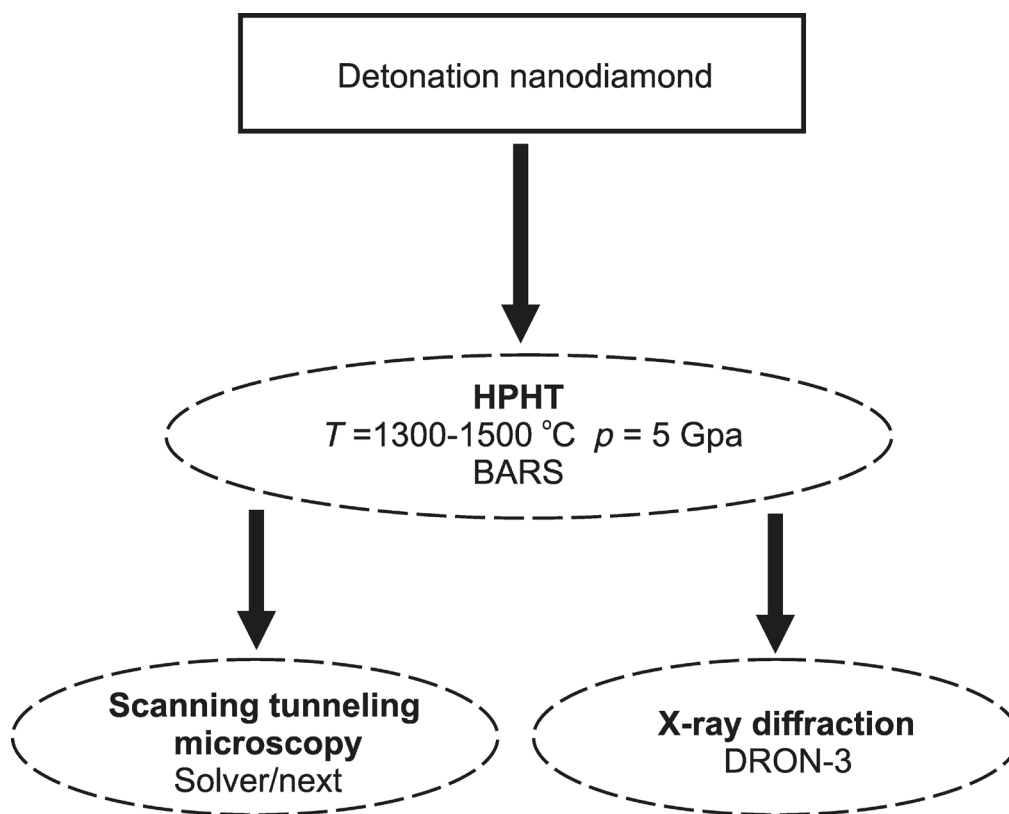
Supplementary Material

Fig. S1. Methods and equipment used in the experiments.